Politecnico di Torino

Porto Institutional Repository

[Article] Physics-Based Mixed-Mode Reverse Recovery Modeling And Optimization Of Si PiN And MPS Fast Recovery Diodes

(Article begins on next page)
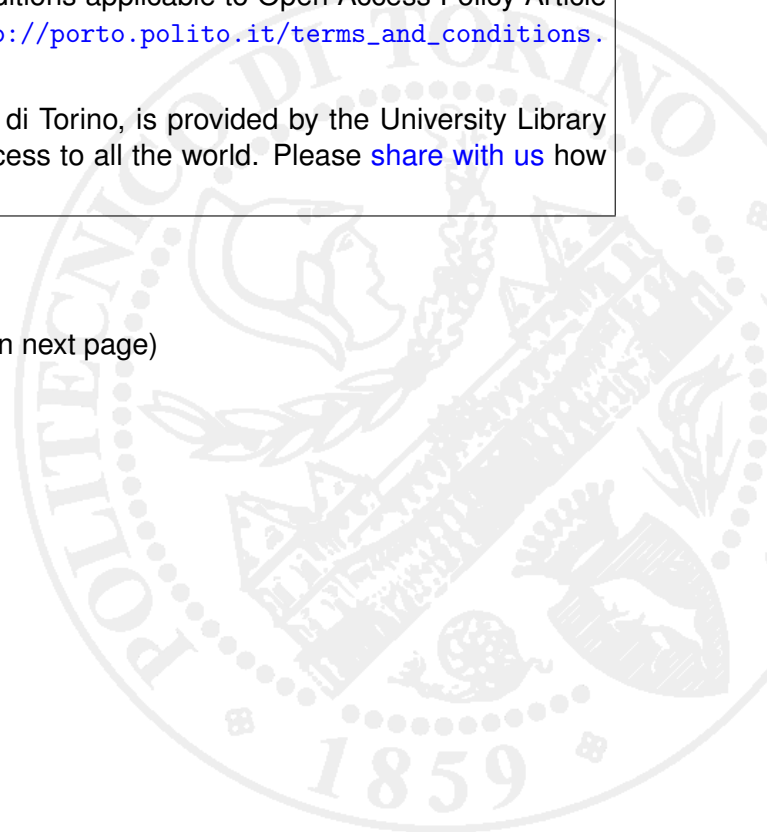
Physics-based mixed-mode reverse recovery modeling and optimization of Si PiN and MPS fast recovery diodes

F. Cappelluti [a,*], F. Bonani [a], M. Furno [a], G. Ghione [a], R. Carta [b], L. Bellemo [b], C. Bocchiola [b], L. Merlin [b]

[a] *Dipartimento di Elettronica, Politecnico di Torino, Corso Duca degli Abruzzi 24, Torino, Italy*
[b] *International Rectifier, Via Liguria 49, 10071 Borgaro, Torino, Italy*

Abstract

The paper presents the results of the application of physics-based mixed-mode simulations to the analysis and optimization of the reverse recovery for Si-based fast recovery diodes (FREDs) using Platinum (Pt) lifetime killing. The trap model parameters are extracted from Deep Level Transient Spectroscopy (DLTS) characterization. The model is validated against experimental characterization carried out on the current International Rectifier (IR) FRED PiN technology. Improved designs, using emitter control efficiency and merged PiN–Schottky structures, are analyzed. Comparison between simulated and measured results are presented.

1. Introduction

High frequency switching applications require fast recovery diodes with high performance in terms of static and dynamic loss; moreover, soft recovery is needed in order to comply with EMC specifications. These requirements should also be matched with the market demand of low cost devices, which make it essential to develop a simple, efficient and low-cost process for device manufacturing. Reliable CAD tools, combining a rigorous model for the device physics and an accurate description of the circuit switching conditions, are indispensable today for device design and optimization.

In this paper, we show the results of the application of mixed-mode simulations to the evaluation of the reverse recovery curve for Si-based FREDs with reference to two device structures, i.e. PiN and merged PiN–Schottky (MPS) diodes. Simulations are carried out exploiting SILVACO mixed-mode module [1], where the device is described through the standard drift-diffusion physics based transport model.

The model has been validated against experimental characterization, both in DC and AC conditions, carried out on a Si FRED based on the current IR technology [2]. The P^+–i–N^+ diode has a 61 µm long, 2×10^{14} cm^{-3} n-doped epilayer.

The doping level for anode and cathode is about 10^{19} cm^{-3}, with anode and cathode junctions depth of 6 and 56 µm, respectively. The device, with a die area of 0.0645 cm^2, has a specified current rating of 8 A. Platinum lifetime killing is used to improve the diode recovery characteristics. After anode and cathode regions formation by diffusing B and P dopant with furnaces, a 10 Å Pt layer is evaporated on the wafer backside and then thermally diffused.

We investigated two different Pt diffusion conditions, in order to assess the impact of lifetime killing on the device performance:

- Pt1: Pt drive in at $T = 880\,°C$, diffusion time $= 40$ min.
- Pt2: Pt drive in at $T = 940\,°C$, diffusion time $= 40$ min.

Besides the standard IR process, we also considered an improved design for the anode aimed at achieving better recovery performance by exploiting a lower doping level (weak anode device).

2. Model description

The physics-based 2D numerical model [1] exploits the standard drift-diffusion approach, including mobility dependence on doping, local carrier concentration, and temperature [3], mobility dependence on electric field, bandgap narrowing, and Auger recombination. The agreement between measured and simulated I–V forward characteristics for a sample without
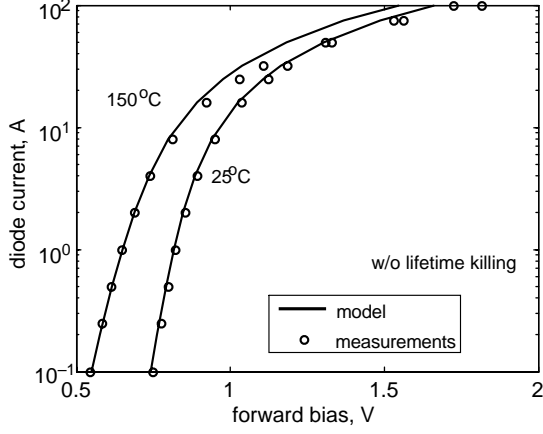
---

* Corresponding author.

Fig. 1. Measured and simulated forward I–V characteristics for an IR PiN diode without Pt lifetime killing.

of space charge density in the semiconductor by including the ionized trap density in the Poisson equation [1].

In DC operation (1) is discarded from the model, and the carrier net recombination rate in the continuity equations becomes

$$R_{\mathrm{SRH},k} = \frac{pn - n_{\mathrm{i}}^2}{\tau_{n0,k}\left(p + \frac{1}{g_k}p_{1,k}\right) + \tau_{p0,k}(n + g_k n_{1,k})} \qquad (6)$$

where n_{i} is the intrinsic carrier concentration, g_k is the trap degeneration factor, $\tau_{n0,k}$ and $\tau_{p0,k}$ are the high-injection carrier lifetimes, related to the temperature-dependent capture cross-sections and the trap density through:

$$\tau_{\{n0,p0\},k}(T) = \frac{1}{v_{\mathrm{th}\,n,p}\sigma_{\{n,p\},k}(T)N_{\mathrm{t},k}}. \qquad (7)$$

Trap energy levels introduced by Pt diffusion and their recombination properties were identified from junction DLTS at $T = 300$ K [6]. The trap concentration was computed from the DLTS signal peaks, whereas the energy level and capture cross-section were derived from the Arrhenius plots of the measured emission rates. For the evaluation of capture cross-sections the density of state mass m^* in the thermal velocity expression has been taken equal to $1.076 \cdot m_0$ and $0.556 \cdot m_0$ for electrons and holes, respectively. Sample Pt1 presented two dominant centers: the acceptor-like level at $E_{\mathrm{c}} - E_{\mathrm{t}} = 0.21$ eV (EF1) and the donor-like level $E_{\mathrm{t}} - E_{\mathrm{v}} = 0.33$ eV (HF1). Sample Pt2 exhibited a significantly increased concentration of HF1 at the expense of EF1, which was almost undetectable. Moreover, a second donor-like trap level (HF2) at $E_{\mathrm{t}} - E_{\mathrm{v}} = 0.27$ eV with significant concentration appeared. All the trap levels have been included in the simulation; their recombination parameters (E_{t}, N_{t} and $\sigma_{p,n}(300\ \mathrm{K})$) as determined by DLTS measurements are summarized in Table 1 [7]. Electron (hole) cross-section of donor (acceptor) like levels were not measured; they have been evaluated from the ratio between electron and holes capture rates c_n/c_p at $T = 300$ K reported in [8,9]. In particular, we have considered $c_n/c_p \approx 1.1$ for the HF1 level, and $c_n/c_p \approx 1.66$ for the EF1 level. Finally, the temperature dependence of capture cross-sections has been modelled as:

$$\sigma_{n,p}(T) = \sigma_{n,p}(300)\left(\frac{T}{300}\right)^{\gamma_{n,p}} \qquad (8)$$

with $\gamma_n = -4$, $\gamma_p = -0.089$ for the HF1 level and $\gamma_n = 2$, $\gamma_p = -4.4$ for the EF1 level, as reported in [9]. For the HF2 level, we have assumed the same capture rate ratio and temperature dependence as the HF1 level.

lifetime killing proves the accuracy of the used models (see Fig. 1).

Trap centers introduced by Pt diffusion are considered as independent recombination levels, whose recombination and generation rates are described according to the classical Shockley Read Hall (SRH) model [4,1]. For transient simulation Poisson's and free carrier continuity equations are complemented by one rate equation for each trap level [5], here written for positively ionized traps:

$$\frac{\partial n_{\mathrm{t},k}}{\partial t} = R_{n,k} - R_{p,k} \qquad (1)$$

where k is the trap level index, $n_{\mathrm{t},k}$ is the ionized trap density, $N_{\mathrm{t},k}$ is the total trap density, and:

$$R_{n,k} = c_{n,k}[n(N_{\mathrm{t},k} - n_{\mathrm{t},k}) - n_{1,k}n_{\mathrm{t},k}] \qquad (2)$$

$$R_{p,k} = c_{p,k}[-p(N_{\mathrm{t},k} - n_{\mathrm{t},k}) + p_{1,k}n_{\mathrm{t},k}]. \qquad (3)$$

The quantities $n_{1,k}$ and $p_{1,k}$ are given by:

$$n_{1,k} = n_i \exp\left(-\frac{E_{\mathrm{Fi}} - E_{\mathrm{t},k}}{k_{\mathrm{B}}T}\right) \qquad (4)$$

$$p_{1,k} = n_i \exp\left(\frac{E_{\mathrm{Fi}} - E_{\mathrm{t},k}}{k_{\mathrm{B}}T}\right) \qquad (5)$$

E_{Fi} and $E_{\mathrm{t},k}$ being the intrinsic Fermi level and the kth trap energy level in the bandgap, respectively. The capture coefficients $c_{\{n,p\},k}$ are given by the product of the kth trap cross-section $\sigma_{\{n,p\},k}(T)$ and of the carrier thermal velocity $v_{\mathrm{th}\,n,p} = (3k_{\mathrm{B}}T/m^*_{n,p})^{1/2}$. The model also accounts for the change

Table 1

Recombination parameters of the trap centers at $T = 300$ K, as determined by DLTS measurements [7]; in brackets are indicated the trap density values used in the simulations

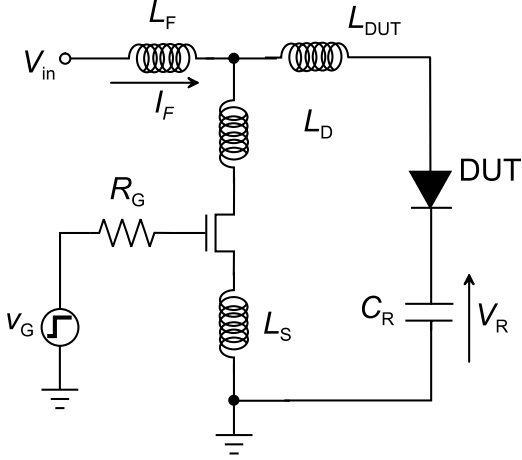| Sample	Pt drive	Energy level (eV)	N_{t} (cm^3)	σ_n (300 K) (cm^2)	σ_n (300 K) (cm^2)
Pt1	880 °C, 40 min	$E_{\mathrm{c}} - E_{\mathrm{t}} = 0.21$	$N_{\mathrm{T,EF1}} = 4\times10^{14}$ (2.5×10^{14})	3.5×10^{-15}	1.52×10^{-15}
		$E_{\mathrm{t}} - E_{\mathrm{v}} = 0.33$	$N_{\mathrm{T,EF1}}/23.5$	4.92×10^{-14}	3.2×10^{-14}
Pt2	940 °C, 40 min	$E_{\mathrm{t}} - E_{\mathrm{v}} = 0.33$	$N_{\mathrm{T,HF2}} = 2\times10^{14}$ (0.58×10^{14})	4.92×10^{-14}	3.2×10^{-14}
		$E_{\mathrm{t}} - E_{\mathrm{v}} = 0.27$	$N_{\mathrm{T,HF2}}/3.1$	1.26×10^{-13}	8.2×10^{-14}

Fig. 2. Circuit schematic of the simulated boost-like converter.

Concerning the recovery behavior, experimental characterization can be carried out by exploiting a large variety of test sets, either commercial or ad hoc circuits. In the present work experimental characterization of reverse recovery was carried out through the tester usually exploited for the extraction of the reverse recovery parameters provided in IR FREDs datasheet [10]. Such test circuit exploits a boost stage reproducing the power factor correction/continuous current mode (PFC–CCM) circuit behavior (a controlled voltage ramp across the diode is applied in order to ensure a soft voltage rising).

As well known, the observed recovery curve is significantly affected by the circuit driving the device under test, therefore an accurate mixed-mode simulation requires a careful modeling of the test circuit. On the other hand, the complexity of the driving circuit deeply impacts on the computation time and, ultimately, on the convergence properties of the simulation. To trade off between these requirements, we chose to simulate the recovery behavior through the boost-like circuit shown in Fig. 2, in which the inductors L_{DUT}, L_D and L_S model parasitic inductances. The MOS device was described through a standard SPICE LEVEL 1 model. Since the circuit is operated in continuous current mode, the input inductor L_F and the output capacitor C_R have been replaced by a constant current source (I_F) and a constant voltage source (V_R), respectively. Circuit parameters, including parasitic induc-tances and MOS parameters, were adjusted in order to accurately reproduce the observed di/dt and dv/dt; in particular, from the dv/dt observed during the first stage of the recovery (before the reverse current peak) we have estimated L_{DUT} = 50 nH. Note that L_{DUT} = 50 nH should not be intended as the diode parasitic inductance only, since it includes parasitic inductances due to the test circuit connections.

3. Results

3.1. PiN diodes

The trap densities extracted from DLTS characterization were adjusted to obtain a good match with measured forward I–V characteristics, at various temperatures, in the case of
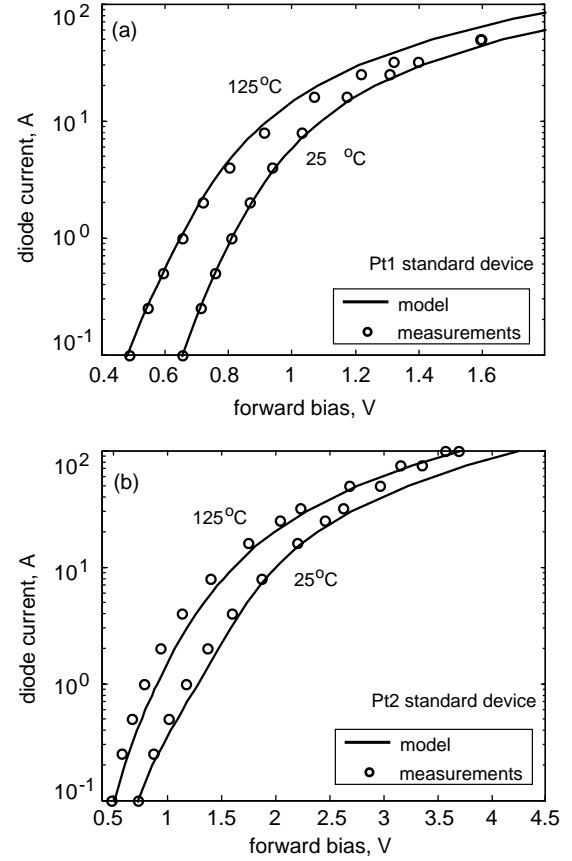

Fig. 3. Measured and simulated forward I–V characteristics for the standard IR PiN diode exploiting lifetime killing: (a) Pt1 device, (b) Pt2 device.

the standard IR FRED. Then, the values used in the simulations, reported in Table 1, were kept constant for all the other analyzed devices. A comparison between simulated and measured forward I–V characteristic of Pt1 and Pt2 PiN diodes is presented in Fig. 3. A good agreement is obtained for the Pt1 diode at both temperatures, confirming the correctness of the assumed temperature dependencies of the trap cross-sections. Concerning the Pt2 diode, the simulations capture the expected trend of the forward voltage drop V_F, due to the increased trap density, but the discrepancy with experimental results is more pronounced. The relative error on V_F at the diode rated current (I_F = 8 A) is about 2 and 8% at T = 25 and 125 °C, respectively (see below for a discussion).

The measured and simulated recovery waveforms (I_F = 8 A , V_R = 200 V, di/dt = 200 A/µs) for device Pt1, at different temperatures, are reported in Fig. 4, supporting the correct extraction of the recombination center parameters carried out on DC data. Fig. 5 shows the comparison between simulated and measured recovery for sample Pt2; for the sake of brevity only the current waveforms is reported. The simulations significantly overestimate the peak current and recovery charge Q_{RR}, with a relative error on Q_{RR} of about 40%. The reason for this discrepancy has not been completely explained at present. Several causes could contribute to it: the possible inaccuracy of trap cross-sections, which have been derived from DLTS measurements; the presence of additional traps, which have
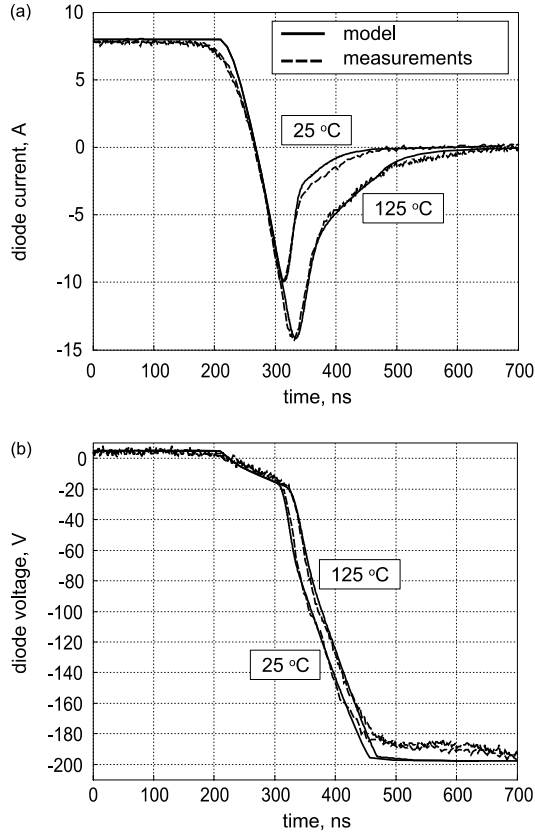
Fig. 4. Measured and simulated recovery waveforms at di/dt = 200 A/µs for Pt1 standard device: (a) current, (b) voltage.

been neglected in the simulation on the basis of an interpretation of DLTS measurements; finally, the inaccuracy of the temperature behavior of cross-sections of HF2, for which the HF1 model has been applied in the absence of any more specific information. Generally speaking, it may be remarked that a good agreement in the DC measured and simulated characteristics does not grant that the transient behavior is accurately modelled. Further work is, therefore, needed to obtain further improvements of the model and model parameter values.
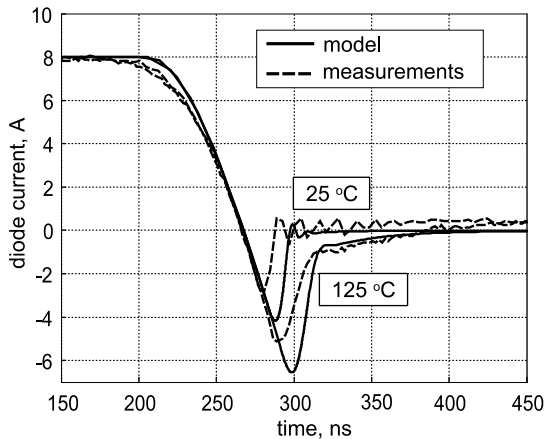

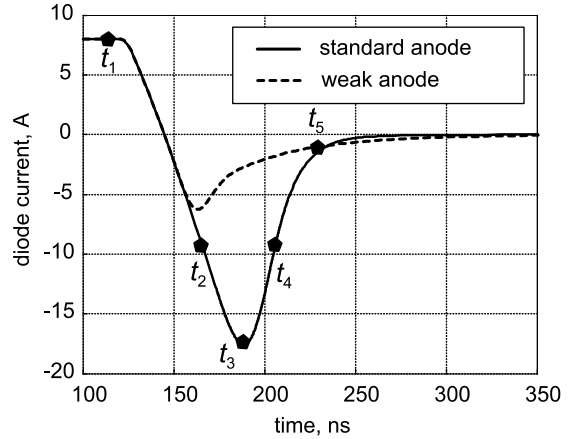Fig. 5. Measured and simulated current recovery waveform at di/dt = 200 A/µs for Pt2 standard device.

Fig. 6. Simulated current recovery waveforms for Pt1 weak anode and standard PiN diodes at T = 25 °C (I_F = 8 A, V_R = 200 V, di/dt = 500 A/µs).

Based on the model extracted from the standard IR technology characterization, the work has been focused on the performance analysis of different PiN diodes, combining Pt lifetime killing and emitter control efficiency [11]. In the new structure the junction depth is reduced to about 3 µm and the emitter doping level is around 10^{16} cm^{-3}. The samples preparation required new technology steps compared to standard devices used initially for model tuning. In this case a weak and shallow anode has been fabricated using B implantation and annealing. High doped 6 µm deep rings are used in the termination to achieve 600 V blocking capability. Devices exploiting both the Pt drive in conditions have been fabricated.

Fig. 6 reports a comparison of the predicted reverse recovery for standard- and weak-anode Pt1 FRED at T = 25 °C. Recovery conditions are I_F = 8 A, V_R = 200 V, di/dt = 500 A/µs. Physics-based simulation allows for an in depth interpretation of the different recovery behaviors shown in Fig. 6, since it yields the time-varying free carrier distributions in the epilayer. The hole carrier densities of the two devices are shown in Fig. 7, where significant time samples are defined on the standard diode recovery curve. For all the other devices the time samples are defined according to the same current levels relatively to I_{rrm}. Concerning the standard diode (Fig. 7 (a)), at the on-state (t_1) injected carriers are almost symmetrically distributed along the drift layer. In the first phase of the recovery (t_2), excess carriers are removed from the boundaries of the drift layer by diffusion and recombination. The maximum reverse current is attained at t_3, when the anode side of the drift layer is depleted from excess carriers. Thereafter, the excess charge is swept out as the depletion region expands in the drift layer starting from both sides of the device (t_4); correspondingly, the diode reverse voltage grows up to the applied value V_R. The recovery current decreases towards zero (t_5) with a slope determined by the dynamics of the depletion. If a significant residual amount of excess charge is present at the cathode side (e.g. Fig. 7 (b)), recombination dominates the excess carrier absorption thus justifying the slow tail in the weak anode current waveform (Fig. 6), in contrast
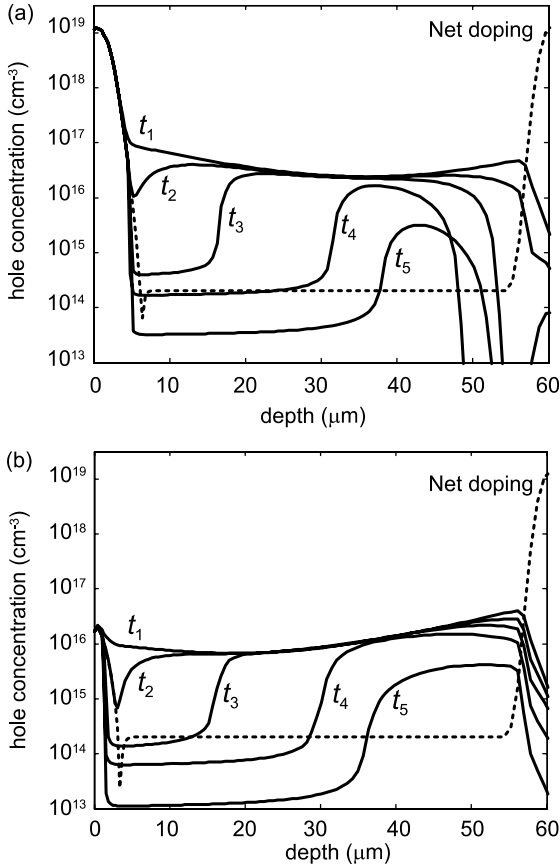
Fig. 7. Carrier decay during reverse recovery in the Pt1 standard (a) and weak anode (b) devices ($I_F=8$ A, $V_R=200$ V, di/d$t=500$ A/µs, $T=25$ °C).

Fig. 8. Carrier decay during reverse recovery in the Pt2 standard (a) and weak anode (b) devices ($I_F=8$ A, $V_R=200$ V, di/d$t=500$ A/µs, $T=25$ °C).

with the steeper behavior of the standard diode where depletion takes place from both sides.

This behavior is even more pronounced in the Pt2 standard anode (see Fig. 8 (a)), where lifetime killing causes a reduced excess charge in the drift region. This in turn determines a stronger depletion from both sides, ultimately resulting in the oscillating behavior shown in Fig. 9. For the weak anode, the reduced carrier injection makes this effect less pronounced, justifying the softer behavior of this device.

Experimental results for Pt1 and Pt2 weak anode diodes are reported in Figs. 10 and 11, respectively. The reverse recovery for a standard sample fabricated on the same wafer is also shown to highlight the improvement achieved with the new design. Typical measured forward voltage drop at the rated current of 8 A was found to be 1.11 and 2.8 V for Pt1 and Pt2 samples, respectively. With respect to the predicted performance, experiments showed less improvement in the reverse recovery, in terms of both peak current and duration. Moreover, the Pt2 weak anode device presents a snappy behavior comparable to that of the standard anode. This discrepancy could suggest a doping level of the anode higher than the one assumed in the simulation. Secondly, a non-uniform distribution of trap density in the drift layer, assumed constant in the simulations, could play a significant role in presence of a low injection efficiency anode. In particular, these results seem to suggest a lower trap density close to the junction, thus locally increasing the carriers'
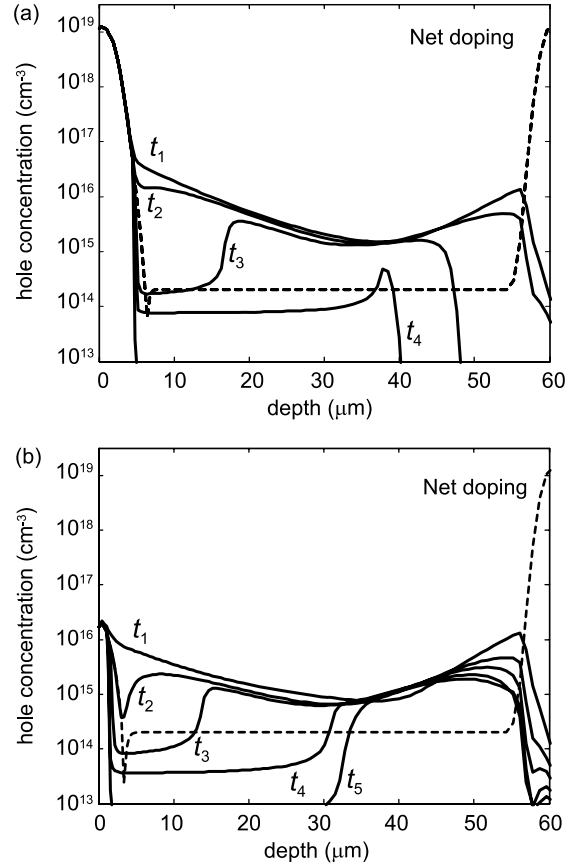
lifetime. This would justify both the higher value of I_{rrm} and the snappy behavior of the actual device. However, further measurements, currently in progress, are required for a final assessment of the matter.

3.2. MPS diodes

Finally, MPS [12] devices, exploiting the weak anode approach, have been investigated. The MPS, Merged
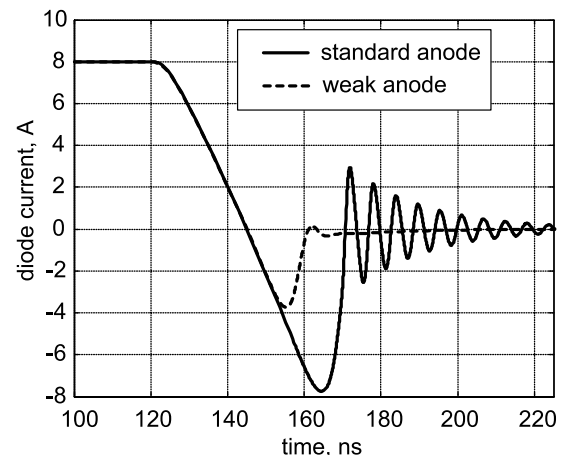

Fig. 9. Simulated current recovery waveforms for Pt2 weak and standard devices at $T=25$ °C ($I_F=8$ A, $V_R=200$ V, di/d$t=500$ A/µs).
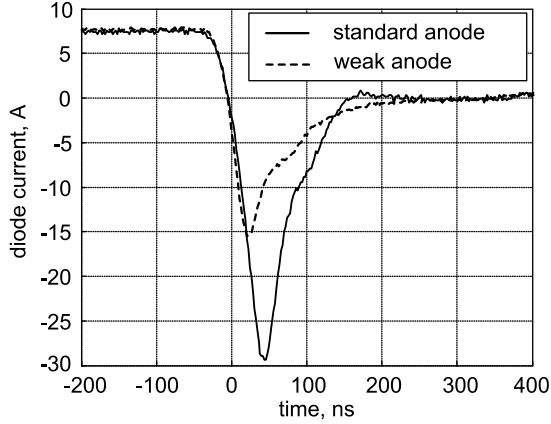
Fig. 10. Measured reverse switching characteristics of Pt1 weak anode and standard devices at $T = 125\ ^\circ$C ($I_F = 8$ A, $V_R = 390$ V, di/d$t = 600$ A/µs).

PiN–Schottky structure, with a well balanced Schottky–PiN area ratio, may allow to reduce and modulate the minority carrier injection driven by the PiN portion of the diode. The voltage forward drop may also be modulated, as well as leakage, by the barrier height. The structures have been fabricated using the standard IR FRED process described in [2], in which the anode mask is replaced with one alternating
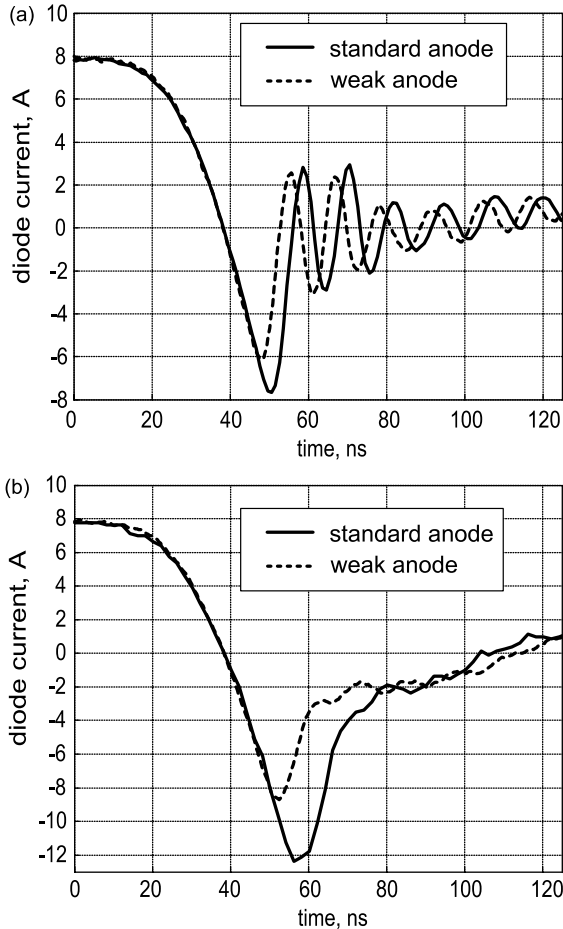

Fig. 11. Measured reverse switching characteristics of Pt2 weak anode and standard devices at $T = 25$ (a) and $T = 125\ ^\circ$C (b) ($I_F = 8$ A, $V_R = 390$ V, di/d$t = 600$ A/µs).
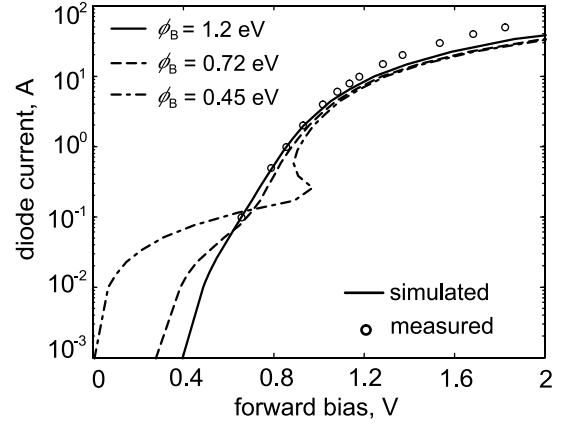

Fig. 12. Comparison between measured and simulated forward I–V characteristics of MPS structure with different Schottky barrier heights ($T = 25\ ^\circ$C).

PiN (B diffused) and Schottky stripes (B not diffused). The Schottky barrier, as well as the ohmic contact on top of the PiN regions, has been obtained by Al deposition and sinter. Two different MPS structures, exploiting the low temperature Pt drive in (Pt1), have been fabricated: the first one (MPS A) has a cell pitch of 18.5 µm, with 17% of Schottky area, the second one (MPS B) has a higher cell pitch (27 µm) and higher percentage Schottky area as well (50%).

The simulated behavior for the MPS A in terms of forward voltage drop is shown in Fig. 12 for different Schottky contact barrier heights. Comparison with the measured data suggests a barrier height higher than the designed one (0.8 eV), as also confirmed from the almost equivalent behavior experimentally observed for the two MPS and the PiN diodes in terms of forward voltage drop, recovery and leakage. In particular, measured reverse currents at $T = 125\ ^\circ$C, $V_R = 600$ V were 6, 21 and 27 µA for the PiN, MPS A and MPS B, respectively.

Fig. 13 shows a comparison of the I–V characteristics for the two MPS and the PiN device, with an assumed barrier height of 0.72 eV. Compared to the PiN diode, MPS A and MPS B shows an increase of the forward voltage drop of about 15 and 27% at the rated current $I_F = 8$ A. On the other hand, as shown in Fig. 14, the MPS structure presents a significantly
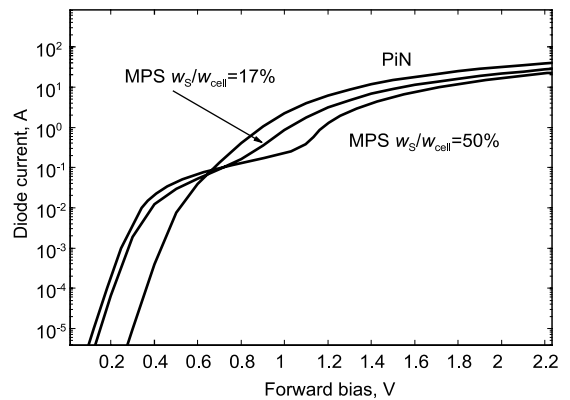

Fig. 13. Simulated forward I–V characteristics for MPS structures with different Schottky areas. Also the weak-anode P–i–N diode is shown, as reference ($T = 25\ ^\circ$C).
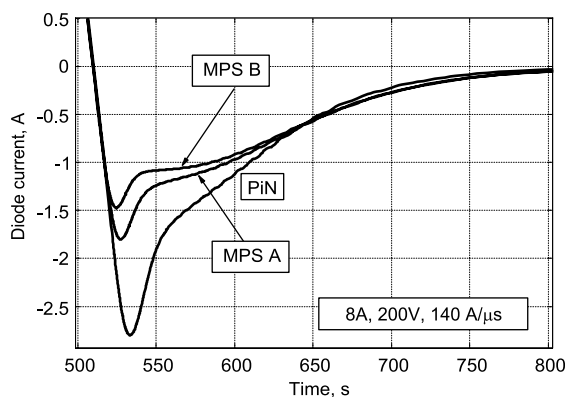
Fig. 14. Simulated reverse switching characteristics for MPS structures with different Schottky areas ($T = 25\,°C$). Also the weak-anode PiN diode is shown, as reference.

lower reverse recovery current with respect to the PiN structure, as lower as larger is the percentage Schottky area. The obtained results are in good agreement with experimental observations reported in the literature [13], and confirm the expected better trade off between forward DC and AC performance achievable with MPS structures.

4. Conclusion

This paper has presented the application of physics-based mixed-mode simulations to the analysis and optimization of the reverse recovery behavior of Si-based FREDs using Pt lifetime killing. The model has been first validated against experimental characterization carried out on the current IR FRED PiN technology. The work has then been focused on the performance analysis of different PiN diodes and MPS structures, combining Pt lifetime killing and emitter control efficiency. On the basis of simulations an improved PiN design with reduced doping level for the anode has been realized, achieving better recovery behavior, both in terms of peak current and duration at the expense of a limited increase of the on-state voltage drop. Physics-based simulation has allowed for an in-depth comprehension of such improvements. Finally, weak anode based MPS structures were investigated: simulations predicted a significant further performance improvement, not experimentally verified, probably due to an unexpectedly high value of the Schottky contact barrier. The presented approach is now being applied to a finer optimization of the IR FREDs combining weak anode design, epilayer optimization and lifetime killing.

References

[1] ATLAS Users Manual, Silvaco International, Santa Clara, CA, 1998.
[2] K. Andoh, S. Fimiani, F. Rue Redda, D. Chiola, Low cost fast recovery diode and process of its manufacture, US Patent 2002/0195613 A1, Dec. 26, 2002.
[3] J. Dorkel, Ph. Leturcq, Carrier mobilities in silicon semi-empirically related to temperature doping and injection level, Solid-State Electron. 24 (1981) 821–825.
[4] W. Shockley, W.T. Read, Statistics of the recombination of holes and electrons, Phys. Rev. 87 (1952) 835–842.
[5] M.T. White III, C.G. Dease, M.D. Pocha, G.H. Kanhaka, Modeling GaAs high-voltage subnanosecond photoconductive switches inn one spatial dimension, IEEE Trans. Electron. Dev. 37 (12) (1990) 2532–2541.
[6] P. Blood, J.W. Orton, The Electrical Characterization of Semiconductors: Majority Carriers and Electron States, Academic Press, London, 1992.
[7] A. Cavallini, Private Communication.
[8] M. Conti, A. Panchieri, Electrical properties of platinum in silicon, Alta Frequenza 40 (1971) 544–546.
[9] R. Siemieniec, M. Netzel, W. Südkamp, J. Lutz, Temperature dependent properties of different lifetime killing technologies on example of fast power diodes, Proc. IETA Conf. (2001).
[10] http://www.irf.com/product-info/datasheets/data/8eth06.pdf.
[11] A. Porst, F. Auerbach, H. Brunner, G. Deboy, F. Hille, Improvements of the diode characteristics using emitter-controlled principles (EMCON-diode), Proc. ISPSD Conf. (1997) 213–216.
[12] B.J. Baliga, H.R. Chang, The merged P-i-N Schottky (MPS) rectifier: a high voltage high-speed power diode, IEDM Tech. Dig. (1987) 658–661.
[13] S.F. Gilmartin, A.F.J. Murray, W.A. Lane, A 1000V Merged P-N/Schottky (MPS) high-speed low-loss power rectifier, IEE Proc. PEVD'98 (1998) 375–380.